Preprints of the 21st IFAC World Congress (Virtual)
Berlin, Germany, July 12-17, 2020

Noise Reduction of Learning Control for Periodic Motion of Galvanometer Scanner

Shingo Ito * **Han Woong Yoo** ** **Georg Schitter** *

* *Christian Doppler Laboratory for Precision Engineering for Automated In-Line Metrology, Automation and Control Institute (ACIN), TU Wien, Vienna A-1040, Austria (email: ito@acin.tuwien.ac.at)*
** *Automation and Control Institute (ACIN), TU Wien, Vienna A-1040, Austria.*

Abstract: For highly precise motion of a galvanometer scanner that tracks a periodic motion reference, learning control significantly decreases the tracking error. To achieve higher quality motion by reducing the angular sensor noise, this paper investigates inversion-based iterative control (IIC) that can learn only at the fundamental and harmonic frequencies of the periodic motion reference. This enables to separate the compensable tracking error from the noise to be eliminated during learning in the frequency domain. The analysis in the paper reveals a tradeoff for the noise reduction in the IIC design, and this paper proposes an equation to quickly tune a design parameter in the tradeoff for better performance. Furthermore, the effectiveness of the IIC algorithm is experimentally demonstrated for a galvanometer scanner. When the galvanometer scanner tracks a 20 Hz triangular motion of ± 10 degrees, the IIC successfully decreases the residual tracking error by 41 % to $2.83 \times \mathbf{10^{-4}}$ deg, by utilizing the noise reduction.

Keywords: Galvanometer scanner, Motion control, Learning algorithms.

1. INTRODUCTION

Highly precise fast scan is indispensable in many applications. To print 3-D objects, for example, a resin is polymerized by scanning a laser spot in the case of direct laser writing [Stampfl et al. (2016)] and stereolithography [Yoo et al. (2019)]. For imaging, a laser spot is scanned over a sample in a confocal microscopy [Pawley (2006)]. In such opto-mechatronic systems, galvanometer scanners are most commonly used to rotate a mirror redirecting a laser beam. A galvanometer scanner consists of a mirror and shaft that are supported by roller bearings and rotated by an electromagnetic actuator with an angular sensor [Matsuka et al. (2016)]. For inspection, the angular motion is usually periodic (e.g. for raster scan) and desired to be highly precise at a high scanning frequency for the high throughput of the system.

There are several challenges to realize the desired scanning motion. Some of them are the nonlinear bearing friction, the mechanical dynamics that limit the control bandwidth, the sensor noise that is typically random to degrade the motion resolution, and the generated heat that increases model uncertainty [Matsuka et al. (2016)]. In order to compensate them, motion control has been proposed for galvanometer scanners. Among different types of motion control for galvanometer scanners (e.g. iterative learning control (ILC) [Yoo et al. (2016)], adaptive control [Zaeh and Pieczona (2018)], and repetitive control [Feng and Zhi (2011)]), inversion-based iterative control (IIC) [Tien et al. (2005); de Rozario et al. (2016)] has advantages for periodic scanning motion.

IIC learns from the motion in the previous trials and updates the control input for the next trial, reducing the motion error, similar to ILC. Unlike ILC, IIC learns in the frequency domain by using discrete Fourier transform (DFT) or Fourier series. Since their coefficients represent signals also in the future, IIC is free from the causality problem and handles scanners' nonminimum phase zeros without restrictions (cf. Yoo et al. (2016)). Furthermore, IIC enables to set the frequencies where the learning takes place in detail. As a result, instead of learning in the entire frequency range, the learning frequencies can be set at the fundamental and harmonic frequencies of the scanning motion. This design freedom is mainly utilized for the reduction of the learning algorithms and the required computation power [Hehn and D'Andrea (2014)] and for stable fast learning of modeling-free IIC [Kim and Zou (2013); Ito et al. (2017)], which is able to compensate for system nonlinearity and model uncertainty [Ito et al. (2019)]. In this paper, another important aspect of learning at the selected frequencies is focused, which is the elimination of the sensor noise between the selected frequencies in learning for high-precision motion. Although this aspect was pointed out [Ito et al. (2017)], the effectiveness has not been investigated for IIC in detail.

This paper proposes a design guideline that takes account of the noise reduction of IIC explicitly, for high-precision

⋆ The financial support by the Christian Doppler Research Association, the Austrian Federal Ministry for Digital and Economic Affairs, the National Foundation for Research, Technology and Development, MICRO-EPSILON MESSTECHNIK GmbH & Co. KG and ATENSOR Engineering, and Technology Systems GmbH is gratefully acknowledged.

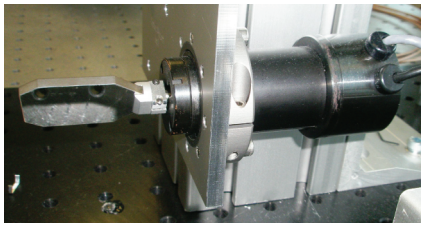

Fig. 1. Photograph of the galvanometer scanner for the experiments.

periodic scanning motion. For detailed evaluations, this paper compares two IIC designs for a galvanometer scanner. The first design is full-spectrum IIC, where the learning takes place for the entire frequency range, and the second design is harmonic-frequency IIC, which learns only at the fundamental frequency of the periodic trajectory and its harmonics.

Section 2 introduces and analyzes a galvanometer scanner, for which IIC is designed and analyzed for the noise reduction in Section 3. Section 4.2 experimentally verifies the the effectiveness of the noise reduction, which is followed by the conclusion in Section 5.

2. SYSTEM DESCRIPTION AND ANALYSIS

2.1 Architecture

Fig. 1 shows the galvanometer scanner (6870M, Cambridge Technology, Bedford, USA) for the experiments. The shaft of the scanner is supported by bearings and rotated by an electromagnetic motor. The motor is driven by a custom-made current amplifier with a bandwidth of about 10 kHz. A mirror is attached on one end of the shaft for steering the laser. On the other end, the motor is attached together with a capacitive angular sensor that measures the shaft angle.

The motion control is implemented by a rapid prototyping control system (DS1005, dSpace GmbH, Paderborn, Germany) at a sampling frequency of 20 kHz. The rapid prototyping control system is also used for data acquisition at the same sampling frequency. The amplifier and the angular sensor are connected to the rapid prototyping control system via a 16-bit DAC (DS2102, dSpace) and 16-bit ADC (DS2004, dSpace), respectively. The resolution of the angular measurement due to least significant bit (LSB) of the ADC is 3.73×10^{-4} deg.

2.2 Feedback control and modeling

Due to the bearings' friction force that is nonlinear and uneven dependent on the rotational angle [Armstrong-Hélouvry et al. (1994)], the shaft can drift away during scanning. In order to prevent it, feedback control is used to stabilize the scanner without a steady-state tracking error. Fig. 2(a) shows a block diagram of the closed-loop system, where $C(s)$ is a phase lead compensator cascaded with a PI controller [Ito et al. (2017)]. The controller feeds back the measurement noise n_m of the angular sensor, fluctuating the actual shaft angle θ. For high positioning resolution, the open-loop cross-over frequency is set to a low frequency of 150 Hz in the design of $C(s)$, which is then discretized by

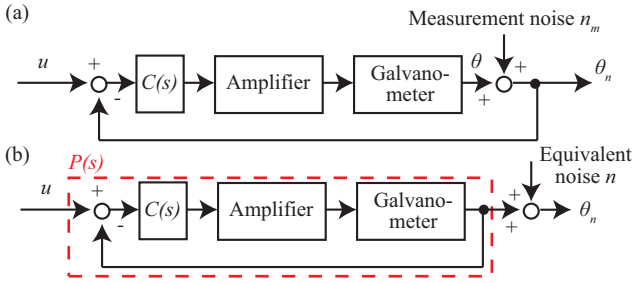

Fig. 2. Block diagram of (a) the galvanometer scanner stabilized by the feedback controller $C(s)$ and (b) the augmented closed-loop system $P(s)$ with the equivalent noise n, where u is the input, and θ_n is the angular sensor output.

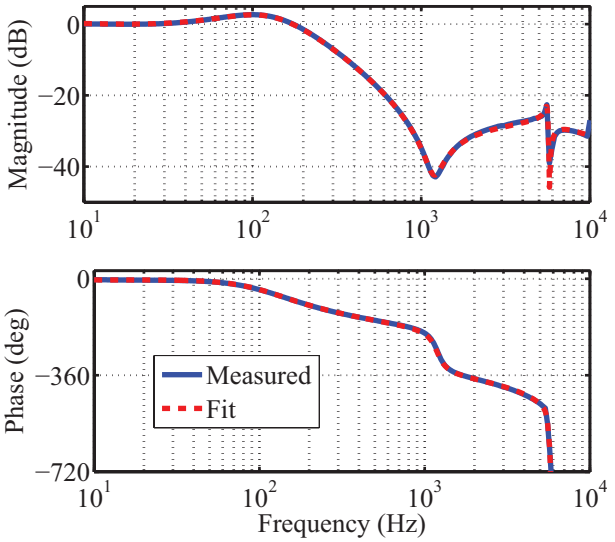

Fig. 3. Measured Bode plot of the stabilized galvanometer scanner $P(s)$ from its input u to the output θ_n. Curve fitting is used to capture the response by a transfer function $\hat{P}(s)$.

the bilinear transformation for implementation. In the rest of the paper, the augmented closed-loop system is denoted by $P(s)$ with the input u, as shown in Fig. 2(b). The sensor output θ_n contains the equivalent measurement noise n, to which the measurement noise n_m is lumped.

To model $P(s)$, a Bode plot from u to θ_n is measured, as shown in Fig. 3. It can be seen that the -3 dB bandwidth of the stabilized system is 225 Hz. For the IIC design in Section 3, the frequency response function (FRF) is captured by fitting an 8th-order transfer function as $\hat{P}(s)$, as shown in Fig. 3. Due to its high order, $\hat{P}(s)$ captures the parasitic dynamics beyond 1 kHz, which may include the torsional mode of the shaft, for the convergence of IIC.

2.3 Measurement noise and ensemble average

For the analysis of the IIC comparison, the noise n is investigated by setting the input u to 0 deg and measuring the sensor output θ_n as n. The results are shown by the blue-solid lines in Fig. 4, where the root-mean square (RMS) value of n is 1.25×10^{-3} deg. The power spectral

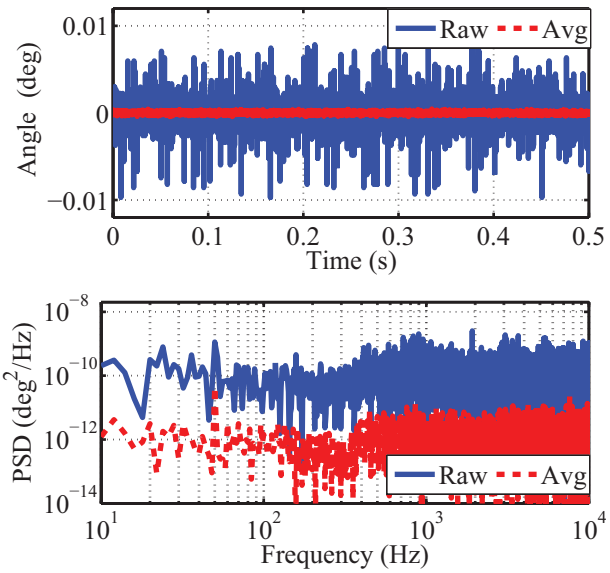

Fig. 4. Measured equivalent noise n and its PSD with and without 100-time ensemble average.

density (PSD) of n is roughly about $10^{-10}\,\mathrm{deg}^2/\mathrm{Hz}$ at low frequencies in Fig. 4(bottom).

For further evaluation, the random components in n are decreased by ensemble average [Karadeniz et al. (2013)]. For this purpose, n is recorded for 0.5 s, and this is repeated N_{en} times. By averaging the N_{en} data points at each sampled time, because the random components are mutually independent for each data set, their PSD is decreased as follows (cf. Jabben and van Eijk (2011))

$$PSD_{r,avg}(j\omega) = PSD_r(j\omega)/N_{en}, \tag{1}$$

where $PSD_r(\omega)$ and $PSD_{r,avg}(\omega)$ are the PSD of the random signal before and after the N_{en}-time ensemble averaging, respectively. Consequently, the RMS is decreased to

$$RMS_{r,avg} = RMS_r/\sqrt{N_{en}}, \tag{2}$$

where RMS_r and $RMS_{r,avg}$ are the RMS of the random signal before and after the ensemble average at the frequency ω, respectively.

The red-dashed lines in Fig. 4 show the results of ensemble average for $N_{en} = 100$. The RMS of the noise is decreased by a factor of 10 to $1.25 \times 10^{-4}\,\mathrm{deg_{rms}}$, and the PSD is entirely lowered to the level of about $10^{-12}\,\mathrm{deg}^2/\mathrm{Hz}$. Since the noise floor is decreased, a peak is clearly visible at 50 Hz, which would be due to the noise from the AC mains.

3. IIC DESIGN AND ANALYSIS

As commonly used for raster scan in imaging systems, a triangular wave with a period of T_r is used as the reference trajectory $r(t)$ in the IIC designs. The block diagram of IIC is shown in Fig. 5. The measured tracking error e_n is recorded for a duration of T_{DFT} and stored in a memory. The buffered data set is used to calculate the discrete Fourier transform (DFT) $E_{n,i}(j\omega)$ of e_n for the frequency ω at the i-th iteration. From the error in the frequency domain, the control input $U_{i+1}(j\omega)$ is generated for the next iteration. By applying the inverse discrete

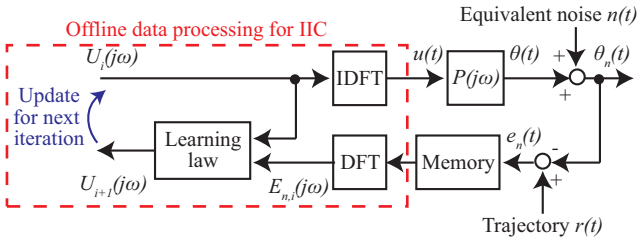

Fig. 5. Block diagram of IIC implemented in the frequency domain. The input noise and the measurement noise are lumped as the equivalent noise n.

Fourier transformation (IDFT), $u(t)$ is obtained in the time domain.

3.1 Full-spectrum IIC

The learning law of typical IIC [Tien et al. (2005); Wu and Zou (2007)] is

$$U_{i+1}(j\omega) = U_i(j\omega) + \rho(j\omega)\hat{P}^{-1}(j\omega)E_{n,i}(j\omega) \text{ for } \omega \le 2\pi f_B, \tag{3}$$

where $\hat{P}(j\omega)$ is the plant model, and f_B denotes the bandwidth. The parameter $\rho(j\omega)$ is the frequency-dependent learning gain, which is tuned for the convergence of IIC [Wu and Zou (2007)]. As the initial condition, $U_0(j\omega)$ is set to zero in this paper. Because the IIC in (3) is active for the entire spectrum up to the bandwidth f_B, it is referred to as full-spectrum IIC hereafter.

3.2 Harmonic-frequency IIC

Since r, u, and θ are correlated, when r is periodic, so is u without the noise n, as follows

$$u(t + T_r) = u(t). \tag{4}$$

Thus, u has frequency components at the fundamental frequency $f_r = 1/T_r$ and its harmonic frequencies for the tracking error compensation. This implies that IIC correctly learns at those frequencies only. The problem of full-spectrum IIC is that the frequency components of θ_n and e_n between the harmonic frequencies contain no useful information for learning, but measurement noise. As a result, the IIC erroneously learns from the noise between the harmonic frequencies, degrading the tracking performance.

To solve the above problem, the noise is eliminated by the following learning law (cf. [Hehn and D'Andrea (2014)]):

$$U_{i+1}(j\omega) = \alpha(j\omega)\left\{U_i(j\omega) + \rho(j\omega)\hat{P}^{-1}(j\omega)E_{n,i}(j\omega)\right\}, \tag{5}$$

using the noise filtering gain $\alpha(j\omega)$

$$\alpha(j\omega) = \begin{cases} 1 & \text{for } \omega = 2\pi f_r, 4\pi f_r, ..., 2\pi l f_r, \\ 0 & \text{otherwise,} \end{cases} \tag{6}$$

where l is a positive integer given by f_B/f_r. Since the IIC is active at the fundamental and harmonic frequencies only, it is referred to as the harmonic-frequency IIC hereafter.

3.3 Tracking error due to noise

The actual tracking error $e = r - \theta$ at the $(i+1)$-th iteration is given from (3) by

$$E_{i+1}(j\omega) = \Phi^{i+1}(j\omega)E_0(j\omega) + \sum_{k=0}^{i} \Phi^k(j\omega)\Psi(j\omega)N_{i-k}(j\omega) \tag{7}$$

where E_i and N_i are the DFT of e and n at i, respectively. The parameter $\Psi(j\omega)$ and $\Phi(j\omega)$ are

$$\Psi(j\omega) = \rho(j\omega)P(j\omega)\hat{P}^{-1}(j\omega), \quad \Phi(j\omega) = 1 - \Psi(j\omega). \tag{8}$$

When the convergence criterion ($|\Phi(j\omega)| < 1$) is satisfied, the first term in the right-hand side of (7) decays away, and the rest of the terms indicate the magnitude of the tracking error due to the noise n, from which the power spectral density of the actual tracking error PSD_e at the $(i+1)$-th iteration is given by

$$PSD_{e,i+1}(j\omega) = \sum_{k=0}^{i} |\Phi|^{2k}(j\omega)|\Psi|^2(j\omega)PSD_n(j\omega). \tag{9}$$

Eq. (9) converges to

$$PSD_e(j\omega) = \frac{|\Psi|^2(j\omega)}{1 - |\Phi|^2(j\omega)}PSD_n(j\omega), \tag{10}$$

where PSD_n is the PSD of n evaluated in Sec. 2.3.

3.4 Noise reduction

When full-spectrum IIC is implemented by (3), the RMS of the converged e is given by

$$RMS_{full} = \sqrt{\int_0^{2\pi f_B} PSD_e(j\omega)\mathrm{d}\omega}, \tag{11}$$

In the case of harmonic-frequency IIC with (5), the IIC learns only at the frequencies selected by α, and the RMS of the converged e is approximated by

$$RMS_{harm} = \sqrt{\sum_{k=1}^{l} \Delta_f PSD_e(j2\pi k f_r)}, \tag{12}$$

using the equivalent noise bandwidth Δ_f [Harris (1978)] given with the recording time T_{DFT} of the data set for the DFT as follows

$$\Delta_f = \Delta_{ENBW}/T_{DFT}, \tag{13}$$

where Δ_{ENBW} is the normalized equivalent noise bandwidth. Dependent on the window function used for the DFT, Δ_{ENBW} typically takes a value between 1 and 2 [Harris (1978)]. For the best noise reduction performance, the rectangle window function is selected, minimizing Δ_{ENBW} to 1 in this paper.

By dividing (12) by (11), the noise reduction ratio R_n in the tracking error by harmonic-frequency IIC is defined by

$$R_n = RMS_{harm}/RMS_{full}. \tag{14}$$

By assuming that $PSD_e(j\omega)$ approximates PSD_e in the vicinity of ω, (14) is simplified by

$$R_n = \sqrt{\frac{\sum_{k=1}^{l} \Delta_f PSD_e(j2\pi k f_r)}{\sum_{k=1}^{l} f_r PSD_e(j2\pi k f_r)}} = \sqrt{\frac{T_r}{T_{DFT}}} = \frac{1}{\sqrt{N_{DFT}}} \tag{15}$$

A concern of the selected window function is the spectral leakage of the tracking error [Verhaegen and Verdult (2007)]. To prevent it, N_{DFT} in (15) should be a positive integer, and it is the number of the r's periods used for the DFT in Fig. 5.

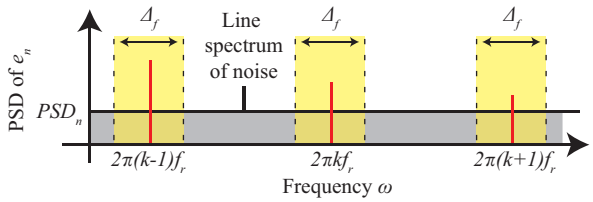

Fig. 6. Conceptual PSD of the measured error e_n around the k-th harmonic frequency of the trajectory r, in the case that e_n includes white Gaussian noise with PSD_n. Periodic noise appears as a line spectrum. The red lines are the compensable tracking error by IIC that occurs at harmonic frequencies of f_r. The signal components in the yellow bands are picked up by harmonic-frequency IIC.

Eq. (15) can be utilized to determine the recording time of e_n in harmonic-frequency IIC. If the buffered data has a length of only one period ($N_{DFT} = 1$), harmonic-frequency IIC attains no noise reduction effect. This is because Δ_f is equal to the fundamental frequency f_r, and the noise between the harmonic frequencies cannot be removed. In contrast, harmonic-frequency IIC can theoretically eliminate all the random noise if the recorded data is infinitely long. In reality, however, a design tradeoff exits to determine N_{DFT} between the noise reduction and the implementable buffer size. In order to quickly achieve a good performance in the tradeoff, (15) is proposed for the tuning of the recording time.

The noise reduction concept is illustrated in Fig. 6, where the compensable tracking error appears as line spectra at harmonic frequencies of f_r. The signal components in the yellow bands are picked up by harmonic-frequency IIC. By increasing N_{DFT}, the yellow bands get narrower for better noise reduction.

4. EXPERIMENTS

4.1 Trajectory and IIC settings

A triangular wave of ± 10 deg and 20 Hz is selected as the motion trajectory r of the galvanometer scanner. To prevent the input saturation of the amplifier, r includes the first 20 harmonics of the triangular wave, as given by the following Fourier series

$$r(t) = A_r \sum_{k=1}^{20} b_k \sin(2\pi f_r k t), \tag{16}$$

using

$$b_k = \frac{8}{\pi^2 k^2} \begin{cases} (-1)^{(k-1)/2} & \text{for odd } k \\ 0 & \text{for even } k, \end{cases} \tag{17}$$

where the amplitude A_r and the frequency f_r take a value of 10 deg and 20 Hz, respectively. Notice that $f_r = 20Hz$ is advantageous in that harmonic-frequency IIC does not pick up the 50 Hz mains noise (Fig. 4).

The modeled frequency response $\hat{P}(j\omega)$ in Section 2.2 is used in the learning law (3) and (5) for full-spectrum IIC and harmonic-frequency IIC, respectively. Since $\hat{P}(j\omega)$ captures the measured frequency response well (Fig. 3), the learning gain $\rho(j\omega)$ is set to one in the entire frequency range.

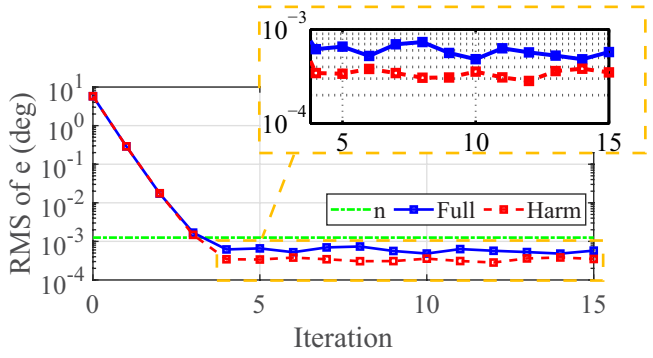

Fig. 7. Measured learning transient of full-spectrum IIC and harmonic-frequency IIC, together with the RMS of the measured equivalent noise n. To evaluate the periodic deterministic error by IICs, 100-time ensemble average is applied to the measured tracking error e_n before its RMS is calculated.

Because the system nonlinearity can deform the scanning motion and create higher harmonics in the tracking error e [Ito et al. (2019)], the IIC bandwidth f_B is set to a sufficiently high frequency of 900 Hz. Since f_r is 20 Hz, this corresponds to $l = 45$ in (6). As a case study, the period number for the DFT is set to $N_{DFT} = 10$ at the implementation.

4.2 Experimental results

Due to the sensor noise, the actual tracking error e cannot be directly obtained for the evaluation of the IICs. Since the tracking error e resulting from the IIC is periodic, 100-time ensemble average is used for θ_n and e_n to improve the signal-to-noise ratio. This ensemble average is used for the evaluation only, and not for the control of the mirror motion.

Fig. 7 shows the measured learning transient of the first 15 iterations, comparing harmonic-frequency IIC and full-spectrum IIC. In both cases, the RMS error quickly converges, and it is smaller than the equivalent noise level. After the convergence, harmonic-frequency IIC shows a smaller error than full-spectrum IIC. The minimum RMS error of harmonic-frequency is $2.83 \times 10^{-4}\,\mathrm{deg_{rms}}$ at the 12th iteration, while that of full-spectrum IIC is $4.82 \times 10^{-4}\,\mathrm{deg_{rms}}$ at the 14th iteration. Reducing the tracking error by 41.3 %, the experiment demonstrates the effectiveness of harmonic-frequency IIC.

The recorded signals at the 12th iteration of the harmonic-frequency IIC and the 14th iteration of the full-spectrum IIC are shown in Fig. 8. The PSD of the control input u in Fig. 8(e) shows that the signal components between the harmonic frequencies are removed by harmonic-frequency IIC, as intended. Fig. 8(b) shows that the tracking error with full-spectral IIC is limited to $\pm 2 \times 10^{-3}$ deg, which is successfully decreased by half by harmonic-frequency IIC. Fig. 8(d) reveals that the reduction is realized by removing the error between the harmonic frequencies. More importantly, the plot also demonstrates that the deactivation of the learning in the frequency bands does not influence the compensation of the deterministic motion error.

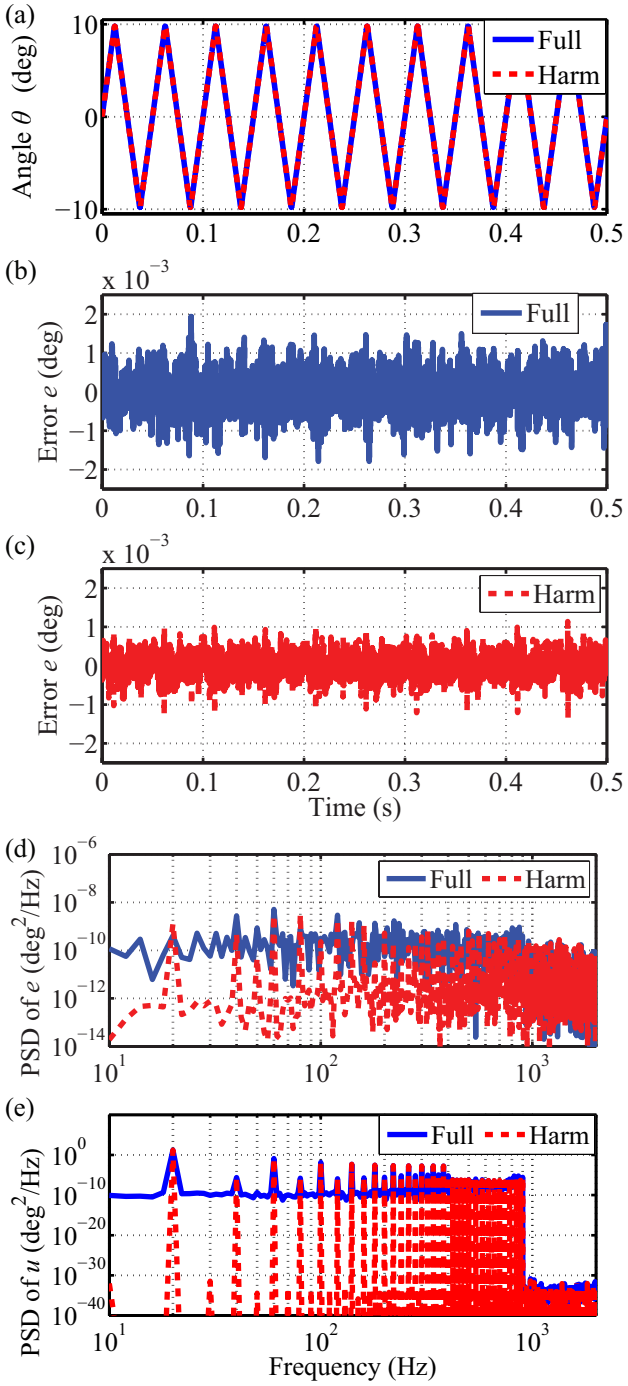

Fig. 8. Measured signals of harmonic-frequency IIC and full-spectrum IIC, respectively: (a) the mirror angle, (b)(c) the tracking error, and (d)(e) the PSD of the tracking error and the control input. Only for evaluation purposes, 100-time ensemble average is applied to θ_n and e_n.

Overall, harmonic-frequency IIC successfully decreases the tracking error by filtering the measurement noise in learning, which is realized by disabling the unnecessary learning within the frequency bands between the harmonic frequencies of the scanning motion.

5. CONCLUSION

This paper investigates the reduction of the measurement noise in IIC by disabling the learning between the harmonic frequencies of a desired periodic motion. For this purpose, standard full-spectrum IIC and harmonic-frequency IIC are analytically and experimentally compared for a galvanometer scanner. The analysis reveals that the noise reduction is related to the recording time of the measured data for the IIC training. Furthermore, the experiments clearly confirm the effectiveness of the learning deactivation between the harmonic frequencies. When a data set of 500 ms is used at each iteration to track a 20 Hz triangular trajectory of ± 10 deg, full-spectrum IIC achieves a tracking error of $4.82 \times 10^{-4}\,\mathrm{deg_{rms}}$. By using harmonic-frequency IIC, the residual tracking error is successfully reduced by 41.3 % to $2.83 \times \mathbf{10^{-4}}$ deg.

ACKNOWLEDGEMENTS

The authors would like to thank Mr. Stefan Pirker for his help during building the experimental setup.

REFERENCES

Armstrong-Hélouvry, B., Dupont, P., and Canudas de Wit, C. (1994). A survey of models, analysis tools and compensation methods for the control of machines with friction. *Automatica*, 30(7), 1083 – 1138. doi: http://dx.doi.org/10.1016/0005-1098(94)90209-7.

de Rozario, R., Fleming, A.J., and Oomen, T. (2016). Iterative control for periodic tasks with robustness considerations, applied to a nanopositioning stage. *IFAC-PapersOnLine*, 49(21), 623 – 628. doi: 10.1016/j.ifacol.2016.10.670. 7th IFAC Symposium on Mechatronic Systems.

Feng, J. and Zhi, J. (2011). Digital implementation of a galvanometric optical scanner based on dsp and fpga. In *2011 International Conference on Mechatronic Science, Electric Engineering and Computer (MEC)*, 1899–1902. doi:10.1109/MEC.2011.6025857.

Harris, F.J. (1978). On the use of windows for harmonic analysis with the discrete fourier transform. *IEEE Proceedings*, 66(1), 51–83. doi:10.1109/PROC.1978.10837.

Hehn, M. and D'Andrea, R. (2014). A frequency domain iterative learning algorithm for high-performance, periodic quadrocopter maneuvers. *Mechatronics*, 24(8), 954 – 965. doi:10.1016/j.mechatronics.2014.09.013.

Ito, S., Troppmair, S., Lindner, B., Cigarini, F., and Schitter, G. (2019). Long-range fast nanopositioner using nonlinearities of hybrid reluctance actuator for energy efficiency. *IEEE Transactions on Industrial Electronics*, 66(4), 3051–3059. doi:10.1109/TIE.2018.2842735.

Ito, S., Yoo, H.W., and Schitter, G. (2017). Comparison of modeling-free learning control algorithms for galvanometer scanner's periodic motion. In *IEEE International Conference on Advanced Intelligent Mechatronics*, 1357–1362. doi:10.1109/AIM.2017.8014207.

Ito, S., Troppmair, S., Cigarini, F., and Schitter, G. (2019). High-speed scanner with nanometer resolution using a hybrid reluctance force actuator. *IEEJ Journal of Industry Applications*, 8(2), 170–176. doi: 10.1541/ieejjia.8.170.

Ito, S., Unger, S., and Schitter, G. (2017). Vibration isolator carrying atomic force microscopes head. *Mechatronics*, 44, 32–41. doi:10.1016/j.mechatronics.2017.04.008.

Jabben, L. and van Eijk, J. (2011). Dynamic error budgeting. *Mikroniek*, 51, 5–12.

Karadeniz, H., Saka, M.P., and Togan, V. (2013). *Introduction to Random Vibration and Stochastic Analysis*, 121–176. Springer London.

Kim, K.S. and Zou, Q. (2013). A modeling-free inversion-based iterative feedforward control for precision output tracking of linear time-invariant systems. *IEEE/ASME Transactions on Mechatronics*, 18(6), 1767–1777. doi: 10.1109/TMECH.2012.2212912.

Matsuka, D., Tanaka, T., and Iwasaki, M. (2016). Thermal demagnetization compensation for fast and precise positioning in galvanometer scanners. *IEEE Transactions on Industrial Electronics*, 63(9), 5514–5522. doi: 10.1109/TIE.2016.2561878.

Pawley, J. (2006). *Handbook of Biological Confocal Microscopy*. Springer US, 3 edition. doi:10.1007/978-0-387-45524-2.

Stampfl, J., Liska, R., and Ovsianikov, A. (2016). *Multiphoton Lithography: Techniques, Materials and Applications*. Wiley-VCH.

Tien, S., Zou, Q., and Devasia, S. (2005). Iterative control of dynamics-coupling-caused errors in piezoscanners during high-speed AFM operation. *IEEE Transactions on Control Systems Technology*, 13(6), 921–931. doi: 10.1109/TCST.2005.854334.

Verhaegen, M. and Verdult, V. (2007). *Filtering and System Identification*. Cambridge University Press.

Wu, Y. and Zou, Q. (2007). Iterative control approach to compensate for both the hysteresis and the dynamics effects of piezo actuators. *IEEE Transactions on Control Systems Technology*, 15(5), 936–944. doi: 10.1109/TCST.2007.899722.

Yoo, H.W., Kerschner, C.J., Ito, S., and Schitter, G. (2019). Iterative learning control for laser scanning based micro 3D printing. In *IFAC Symposium on Mechatronic Systems*.

Yoo, H.W., Ito, S., and Schitter, G. (2016). High speed laser scanning microscopy by iterative learning control of a galvanometer scanner. *Control Engineering Practice*, 50, 12–21. doi:10.1016/j.conengprac.2016.02.007.

Zaeh, M. and Pieczona, S. (2018). Adaptive inverse control of a galvanometer scanner considering the structural dynamic behavior. *CIRP Annals*, 67(1), 385 – 388. doi: 10.1016/j.cirp.2018.04.063.